

Microstructures of SiC nanoparticle-doped MgB₂/Fe tapes

Y. Zhu

Department of Materials Science and Engineering, University of Wisconsin-Madison, Madison, Wisconsin 53706-1595

A. Matsumoto

Applied Superconductivity Center, University of Wisconsin-Madison, Madison, Wisconsin 53706 and National Institute for Materials Science, Tsukuba, Ibaraki 305-0047, Japan

B. J. Senkowicz^{a)}

Applied Superconductivity Center, University of Wisconsin-Madison, Madison, Wisconsin 53706

H. Kumakura and H. Kitaguchi

National Institute for Materials Science, Tsukuba, Ibaraki 305-0047, Japan

M. C. Jewell

Applied Superconductivity Center, University of Wisconsin-Madison, Madison, Wisconsin 53706

E. E. Hellstrom and D. C. Larbalestier^{a)}

Department of Materials Science and Engineering, University of Wisconsin-Madison, Madison, Wisconsin 53706-1595 and Applied Superconductivity Center, University of Wisconsin-Madison, Madison, Wisconsin 53706

P. M. Voyles^{b)}

Department of Materials Science and Engineering, University of Wisconsin-Madison, Madison, Wisconsin 53706-1595

(Received 5 April 2007; accepted 16 May 2007; published online 11 July 2007)

We have studied bulk MgB₂ synthesized by reaction of MgH₂ and B with and without SiC nanoparticles and at a range of reaction temperatures. All of the samples showed enhanced upper critical fields compared to most bulk MgB₂, including the sample with 10 at. % SiC reacted at 600 °C, which showed $H_{c2}(0\text{ K}) > 42\text{ T}$. Extensive transmission electron microscopy (TEM) and STEM observations show that using MgH₂ instead of pure Mg reduces the concentration of oxide second phases in the tapes, but that adding SiC reintroduces nanoscale grains of MgO, SiO₂, and SiO_xC_y, and larger grains of Mg₂Si. SiC causes some C doping of the MgB₂, but electron energy loss spectroscopy and x-ray diffraction measurements show that the C concentration is similar to other bulk C-doped MgB₂. In all the samples with and without SiC, the grain size is very small, 10–60 nm. Electron scattering from the high density of grains and second-phase boundaries is responsible for the enhanced H_{c2} of these samples. However, the H_{c2} properties are somewhat compromised by very broad transitions that may have their origin in the local variations of nanostructure. © 2007 American Institute of Physics. [DOI: 10.1063/1.2750409]

I. INTRODUCTION

The relatively high critical temperature T_c and low raw material cost of MgB₂ make it a potential competitor to conventional Nb-based superconductors. Since large-scale superconducting magnet applications require long lengths of conductors with high critical current density J_c and upper critical magnetic field H_{c2} , a number of synthesis techniques with different impurities have been developed to improve the properties of MgB₂. However, MgB₂ has been proven to be generally resistant to doping except with C and Al. Adding C to MgB₂ using various bulk processing routes has been shown to increase H_{c2} .¹ So far the highest reported $H_{c2}^{\parallel ab}$ (0 K) is ~35 T for C-doped MgB₂ wires or bulks,^{1,2} and over 40 T for C-nanotube doped bulk MgB₂.³ In such

samples, C substitutes for B and introduces electron scattering which reduces the mean free path and the coherence length ξ , increasing H_{c2} .^{2–5} The highest $H_{c2}^{\parallel ab}$ (0 K) in C-doped MgB₂ thin films exceeds 70 T,⁵ but the difference between MgB₂ bulk and thin films is not yet understood.

Adding SiC in the form of nanoparticles to bulk MgB₂ proved particularly effective at enhancing the superconducting properties.^{6,7} The SiC nanoparticles decompose at typical bulk MgB₂ synthesis temperatures, and (among other possible effects) are believed to act as a source of C doping.⁸ The solubility of Si in MgB₂ is very small: at the very high temperatures and pressures necessary to synthesize single-crystal MgB₂, C is incorporated into the MgB₂ lattice, but Si is not.⁴ Besides increasing H_{c2} , adding SiC to bulk MgB₂ also significantly improves J_c at high fields,⁶ perhaps by introducing a high density of structural nanodefects and nanoscale precipitates.⁸ Defects with the dimension 2–4 nm have been observed in SiC-doped MgB₂ bulks,⁹ which are believed to cause strong scattering and enhance both J_c and

^{a)}Current address: Applied Superconductivity Center at National High Magnetic Field Laboratory, Florida State University, Tallahassee, FL 32310.

^{b)}Corresponding author; electronic mail: voyles@engr.wisc.edu

H_{c2} . The size of the SiC particles also has an effect: using smaller SiC particles leads to higher H_{c2} and irreversibility field H_{irr} in MgB₂ wires.¹⁰ Although some microstructural characterization work has been done in SiC-doped MgB₂,^{8,9,11} the presence of many chemical phases and their very small size makes complete characterization challenging, and the best ways to optimize the superconducting properties of SiC-doped MgB₂ are still far from fully understood.

Here we extended our study of a set of samples in which we previously reported $H_{c2}(0\text{ K}) > 42\text{ T}$, significantly higher than the maximum values of 32–35 T found in C-doped single crystals,⁴ chemical vapor deposition (CVD)-doped filaments,² and ball-milled bulks.¹ The samples are SiC-doped MgB₂ tapes fabricated by an *in situ* powder-in-tube (PIT) process using MgH₂ rather than Mg as the reactant for the B.⁷ MgH₂ is believed to reduce O carried to the reaction with the B powder, and to therefore increase J_c by reducing the formation of oxygen-containing second phases, improving the connectivity of the MgB₂ grains.¹² Here we expand on the matrix of earlier electromagnetic characterizations and report a detailed analysis of the microstructures of the MgB₂ tapes as a function of SiC content and reaction temperature. In particular, we show that *in situ* reacted tapes are inhomogeneous on scales of 10–30 nm or less. This adds to the electron scattering responsible for H_{c2} , since the electron mean free path in pure MgB₂ is $\sim 60\text{ nm}$.¹³ Nonsuperconducting phases are present, which can enhance the vortex pinning, but can also strongly degrade the connectivity needed for high critical current density if they cluster at grain boundaries, as recently seen in O-contaminated MgB₂.¹⁴ One conclusion from this study is that MgB₂ is very sensitive to O, whether brought in by B, SiC, or the reaction atmosphere. Until we better understand the fine details of the *in situ* reaction, it may be that many unpredictabilities in the magnitude of $J_c(H, T)$ can be attributed to uncontrolled variations in connectivity and vortex pinning due to the nanometer size MgB₂ grains and reaction products of the Mg and B sources.

II. EXPERIMENTAL DETAILS

The preparation of these samples has been extensively described elsewhere.⁷ To summarize, MgH₂ and B powders were mixed in a 1:2 atomic ratio in an Fe tube, with additions of 0, 5, and 10 at. % of 30 nm diameter SiC nanoparticles and then rolled to a tape. Samples were reacted for 1 h at temperatures of 600, 700, 800, and 900 °C, making a matrix of 12 samples whose properties exhibited systematic trends as a function of doping and reaction temperature. The Fe sheaths were mechanically removed before electromagnetic and microstructural characterization. Resistivity curves were measured in a 9 T Quantum Design physical properties measurement system, a 33 T Bitter magnet at the National High Magnetic Field Lab (NHMFL) in Tallahassee, and a 60 T short pulse magnet at the NHMFL in Los Alamos National Lab. The 10% and 90% points on the resistive transition curves were used to define a transition breadth ΔH and H_{c2}^{\parallel} . Magnetization properties were measured in a 14 T Oxford Instruments vibrating sample magnetometer, from which the critical current density $J_c(H, T)$ was calculated as-

TABLE I. $\rho(40\text{ K})$, RRR, and connectivity data for all samples.

	Reaction temperature	$\rho(40\text{ K})$ ($\mu\Omega\text{ cm}$)	Residual resistivity ratio (RRR)	Active cross section (%)	$H_{c2}^{\parallel}(10\text{ K})$ (T)
0%SiC	600 °C	115.9	1.70	9.0	24.7
	700 °C	69.8	1.97	10.7	
	800 °C	52.8	2.1	12.7	
	900 °C	31.3	2.40	16.6	
5%SiC	600 °C	265.6	1.35	7.4	
	700 °C	166.1	1.54	8.2	
	800 °C	97.7	1.61	8.4	
	900 °C	65.7	1.64	17.4	
10%SiC	600 °C	324.3	1.27	8.2	31.6
	700 °C	199.5	1.39	9.3	
	800 °C	132.3	1.47	11.8	
	900 °C	99.7	1.58	12.7	

suming fully connected samples using the expression $J_c(H, T) = 0.5\Delta M \cdot 12b / (3bd - d^2)$, where b and d are the width and thickness of the rectangular section bar. The electric field criterion of the swept-field measurements was $\sim 1\ \mu\text{V}/\text{cm}$ for the small 2–4 mm sized samples used. The sample connectivity is almost invariably considerably less than one in bulk MgB₂ samples, which has a direct influence on J_c . The connected cross section $1/F$ was calculated using the relation $\rho_n(T) = F[\Delta\rho_{sc}(T) + \rho_n(0)]$, where ρ_n is the normal state resistivity and $\Delta\rho_{sc}(300\text{--}50\text{ K}) = 7.3\ \mu\Omega\text{ cm}$.¹⁵

The microstructure and phases of the sample were characterized by x-ray diffraction (XRD), transmission electron microscopy (TEM), and scanning TEM (STEM). TEM specimens were prepared by mechanical wedge polishing the MgB₂ cores on an Allied TechPrep polishing wheel with the Multiprep sample holder assembly.¹⁶ Samples were thinned to $< 100\text{ nm}$ thick at the edge using diamond plastic lapping films lubricated by denatured alcohol, followed by limited ion milling at $5^\circ\text{--}10^\circ$ angle of incidence with a 5 mA, 5 keV ion beam. Ion milling damage in MgB₂ creates cellular features in the images, which we did not observe. As an additional check for damage, low-resolution TEM observations were also made on mechanically thinned samples without ion milling and no difference was seen. The outer four samples of the matrix (see Table I) were thinned for TEM experiments: 600 °C-pure, 600 °C-10% SiC, 900 °C-pure, and 900 °C-10% SiC, although only images for the SiC-doped samples are shown here.

A CM200 TEM operated at 200 keV was used for bright-field (BF) and dark-field (DF) images. We used the *Particle* package of the DIGITALMICROGRAPH program to measure the grain size from DF TEM images, although contrast from intragrain defects had first to be erased by hand. The reported grain size is the circular approximation diameter to each grain. Several thousand grains were measured for each sample so as to get statistical meaningful size distributions for grains larger than 5 nm. The objective aperture was centered on a portion of the MgB₂ $\{1\bar{1}01\}$ ring in the polycrystalline diffraction pattern, but was large enough to

admit some diffraction from second phases such as MgO. Those second phases are therefore also represented in the grain size distributions.

Chemical microanalysis was performed using Z-contrast STEM imaging, STEM x-ray energy dispersive spectroscopy (EDS), and STEM electron energy-loss spectroscopy (EELS) with a ~ 0.5 nm electron probe on a JEOL-2010F. The Z-contrast image intensity scales as the atomic number of the sample $Z^{1.7}$, projected along the beam direction. For single crystal samples imaged on a zone axis, probe channeling effects complicate the simple interpretation of the image,¹⁷ but for randomly oriented polycrystalline samples, such high-symmetry zone axes occur only rarely. Elemental maps were acquired for Mg, Si, O, and C with a Noran EDS system with a Thermo-Noran Norvar thin window, but the O and C maps are limited by window absorption. EEL spectra and spectrum line scans were acquired with an acquisition time of about 0.2 s/spectrum using a Gatan Imaging Filter. The spacing between spectra in the line scans was 1–7 nm, much larger than the total specimen drift during any of the line scan acquisitions. Elemental distributions were derived from the EELS scans by integrating the corresponding background-subtracted EELS edges, then normalizing by the O K pre-edge background intensity in order to reduce the effects of thickness variations along the scan line. All samples were cleaned with a plasma cleaner before being put into the STEM in order to reduce the surface hydrocarbon contamination. As noted later, there is always some residual hydrocarbon contamination, but incorporating a Si sample with our MgB₂ sample enabled us to estimate the real C content inside the MgB₂ lattice.

III. RESULTS

A. Electromagnetic properties

Table I provides a broad overview of the properties of the 12 sample set. The resistivity ρ exhibits a systematic trend with SiC content and reaction temperature, ranging from a minimum of 31 $\mu\Omega$ cm for the 900 °C-pure to a high of 324 $\mu\Omega$ cm for the 600 °C-10% SiC sample. These values are all far too high to be characteristic of fully connected samples. The Rowell analysis indicates only a small (0.08–0.17) and generally decreasing connectivity as reaction temperature declines or SiC content increases, even though, as seen later, H_{c2} and J_c increase in both cases.

Figure 1 shows T_c and ΔT_c , the difference between the resistive T_c^{onset} and T_c^{zero} , of all 12 samples. Both T_c^{onset} and T_c^{zero} values generally increase with increasing reaction temperature, and ΔT_c increases with increasing SiC concentration at all temperatures, while decreasing with increasing temperature at fixed SiC concentration. However, the maximum onset T_c value is 38 K, not 39 K, even after 900 °C reaction. The resistive transitions T_c and ΔT_c imply that disorder and some incomplete reaction with the added SiC occur for all our samples, which is confirmed by the microstructural results below.

Figure 2(a) shows the H_{c2}^{\parallel} data as a function of temperature, for the four outlying samples in our set: 600 and 900 °C with 0 and 10 at. % SiC. The 600 °C-10% SiC sam-

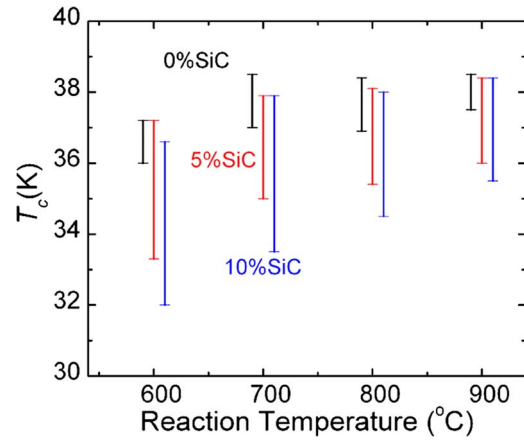


FIG. 1. (Color online) Width of the resistive T_c transitions as a function of reaction temperature and doping level for the entire sample set.

ple's H_{c2} of 42 T at 2.3 K is one of the highest reported values for bulk MgB₂. However, like the T_c transitions, the in-field H_{c2} transitions are also broadened in a systematic way, being both narrower and lower, with lower SiC content and higher reaction temperature as shown in Fig. 2(b). The 10%–90% transitions at 2 K are all very broad, extending from 18 to 22 T for the 900 °C-pure sample but from 27 to 42 T for the 600 °C-10% SiC sample.

The $J_c(H, T)$ data of the samples have been shown elsewhere.⁷ The local J_c of a material is determined by the vortex pinning strength of the microstructure and at high fields by H_{c2} , and some of the J_c data can be understood on this basis. To summarize, for both pure and SiC-doped

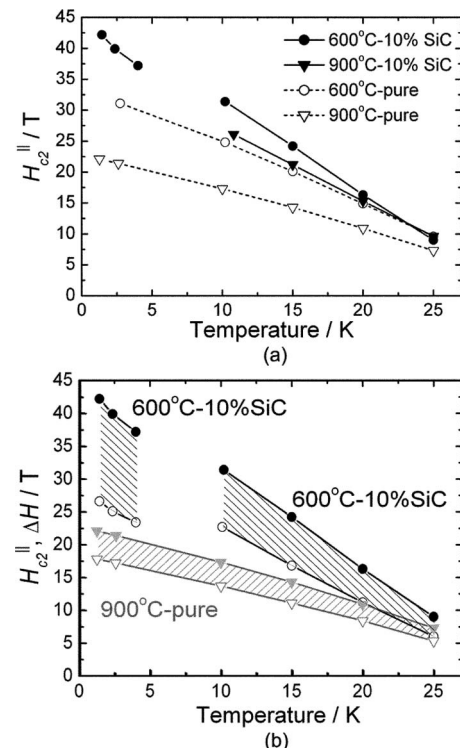


FIG. 2. (a) Upper critical magnetic field H_{c2}^{\parallel} (T) for the samples investigated by TEM. (b) The transition breadth $\Delta H_{c2}(10\% - 90\%)$ as a function of temperature for the 600 °C-10% SiC and 900 °C-pure samples (has been previously published in Ref. 7).

samples, the high-field $J_c(4.2\text{ K})$ values are higher for the lower reaction temperatures which also have higher H_{c2} seen in Fig. 2. Adding SiC increases the low-temperature high-field $J_c(4.2\text{ K}, H > 6\text{ T})$ compared to the pure samples, consistent with the higher H_{c2} of the SiC samples, and 10%SiC samples exhibit $J_c(4.2\text{ K}) \sim 10^4\text{ A/cm}^2$ at 10 T. However, the absolute magnitude of J_c in these samples is strongly reduced by the low connectivity of the superconducting grain structure, indicated by their unphysically high normal state resistivities $\rho(40\text{ K})$ in Table I.

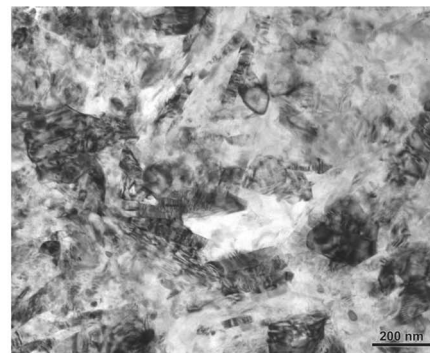
Most of the electromagnetic results are summarized in Table I. The fact that the trends are systematic with respect to the addition of SiC or the change of reaction temperature indicates that they arise from those deliberate changes, not the uncontrolled variability which can plague some forms of MgB_2 synthesis.

B. Microstructures

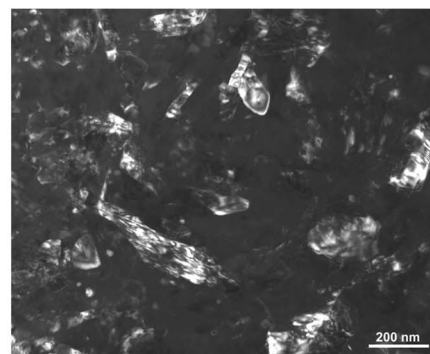
Figure 3 shows a BF image and the corresponding DF image taken from the 900 °C-10%SiC sample. The MgB_2 grains are small, and most grains show a lot of interior contrast generated by intragrain defects. Figure 3(c) shows the grain size distributions derived from DF TEM images similar to that in Fig. 3(b), while Table II gives the average grain size for each sample. All four samples show a large portion of grains less than 50 nm in diameter. Table II shows that doped samples have smaller grain size than pure samples, as seen also in the distribution plot [Fig. 3(c)] for the 900 °C samples. Although the 900 °C samples have about twice the grain size of the 600 °C samples, they are barely smaller for the SiC-doped ones than for the pure. In both cases the grain size remains very small, whether at 600 °C (29 and 27 nm) or at 900 °C (54 and 48 nm).

There are a number of second phases present in SiC-doped MgB_2 samples. Figure 4(a) shows a selected-area-diffraction (SAD) pattern taken from the 600 °C-10%SiC sample in which the $\text{MgO}\{111\}$ diffraction is clearly visible. Similar MgO diffraction was observed in the 900 °C-10%SiC sample; MgO is ubiquitous in both doped samples. The MgO grains are quite small and uniformly distributed over the few-hundred nanometer length scales probed by SAD. In the pure samples, the MgO diffraction ring is much weaker and in some cases not present at all, as shown in Fig. 4(c). Figure 4(b) shows a large Mg_2Si grain which is identified from its SAD pattern. The Mg_2Si we observed in these samples is in the form of single crystals $\geq 300\text{ nm}$, much larger than average MgB_2 grain size. Such large Mg_2Si grains have also been reported in literature⁹ although the mechanism to form large Mg_2Si from nanoscale SiC particles is unclear.

Figure 5 shows a Z-contrast image of the 600 °C-10%SiC sample. If there are no large changes in thickness at very short length scales, which is usually true for small areas in TEM samples, the intensity difference in an image such as Fig. 5 comes from differences in local sample chemistry. Table III summarizes the predicted Z-contrast intensities for various phases that might be present in this sample, relative to the intensity of MgB_2 . Thus, while Mg_2Si



(a)



(b)

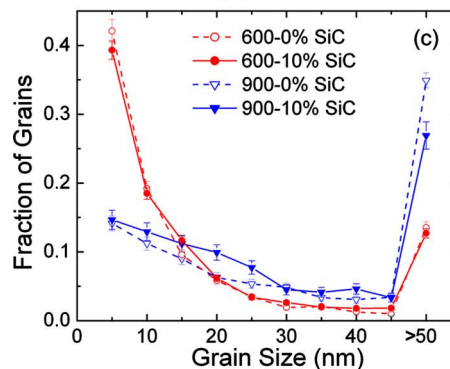


FIG. 3. (Color online) (a) BF and (b) DF TEM images of the 900 °C-10%SiC sample. The DF image is formed with an aperture centered on part of the $\text{MgB}_2\{1\bar{1}01\}$ diffraction ring. (c) Grain size distributions for the samples, measured from TEM DF images similar to (b).

has a higher Z per formula unit than MgB_2 , it also has a larger unit cell, so that its Z -contrast intensity is only slightly higher. Figure 5 shows many domains of different chemistry with the dimension 10–60 nm, which is consistent with our grain size measurement results. Clumps of MgO or SiO_xC_y with size of 10–20 nm are very common, many outlining grains of MgB_2 .

The dark grey regions in Fig. 5 are mostly MgB_2 domains. They make up a majority of the sample and are simi-

TABLE II. Grain size measurement.

	600 °C pure	600 °C 10% SiC	900 °C pure	900 °C 10% SiC
Number of grains measured	2129	3070	1400	867
Average grain size (nm)	29.2	27.3	54.1	47.6

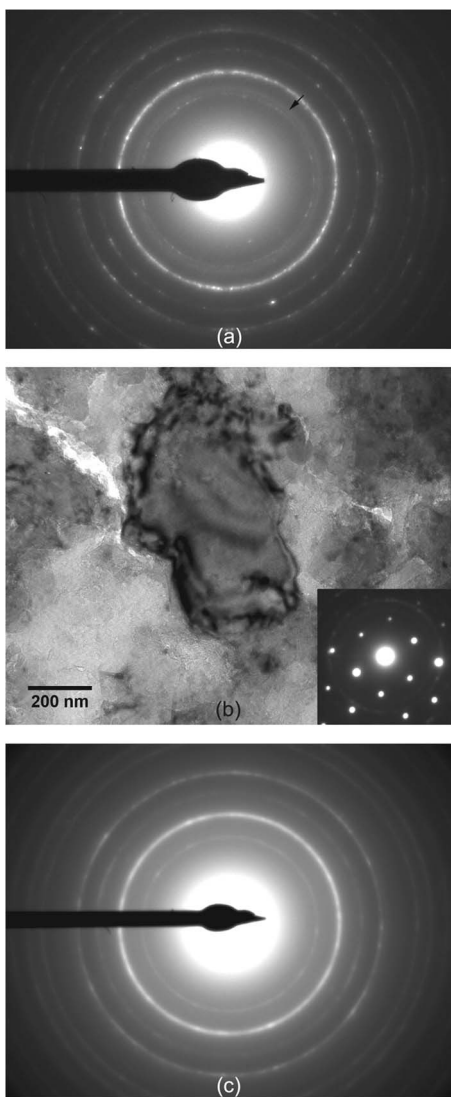


FIG. 4. TEM results from the 600 °C samples. (a) A SAD pattern from the 10%SiC sample with the MgO {111} diffraction ring indicated. (b) A BF TEM image of the 10%SiC sample with a large single crystal Mg₂Si grain at the center. The inset shows the Mg₂Si [110] SAD pattern of that grain. (c) A SAD pattern from the 600 °C-pure sample showing no MgO.

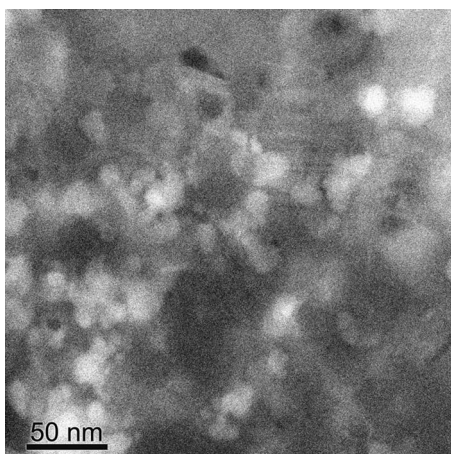


FIG. 5. Z-contrast image taken from 600 °C-10% SiC sample. Bright regions in this image are heavy (high atomic number) phases such as MgO and SiO_xC_y. Dark regions are light phases including MgB₂ and Mg₂Si.

TABLE III. Z-contrast intensity for various phases relative to the intensity of MgB₂.

	MgB ₂	MgB ₂ C ₂	MgO	Mg ₂ Si	SiC	SiO ₂ (quartz)
Z-contrast intensity relative to MgB ₂	1	0.75	1.60	1.03	1.56	1.45

lar in size to the crystal grains found in conventional TEM. Figure 6 shows a Z-contrast image of a single MgB₂ domain in the same sample and its surroundings, together with the B, C, and O EELS edge intensities as a function of position along the line indicated in the figure. The dark grey region is B-rich compared to its surroundings, indicating it is a MgB₂ grain surrounded discontinuously by lighter C- and O-rich regions. Figure 7 shows a similar Z-contrast image, this time with EDS maps of the Mg, Si, and O intensity, again from the 600 °C-10%SiC sample. The Mg signal is uniform across the dark grey region, confirming that it is MgB₂. It is

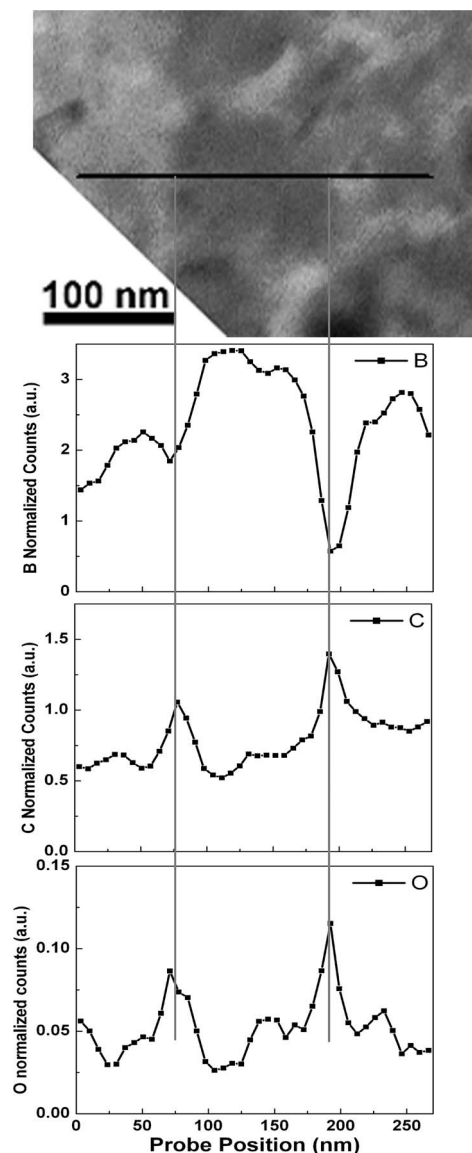


FIG. 6. Z-contrast image taken from 600 °C-10% SiC sample and the B, C, and O elemental distributions from an EELS line scan along the line in the image. EELS spectra were acquired every 6.7 nm.

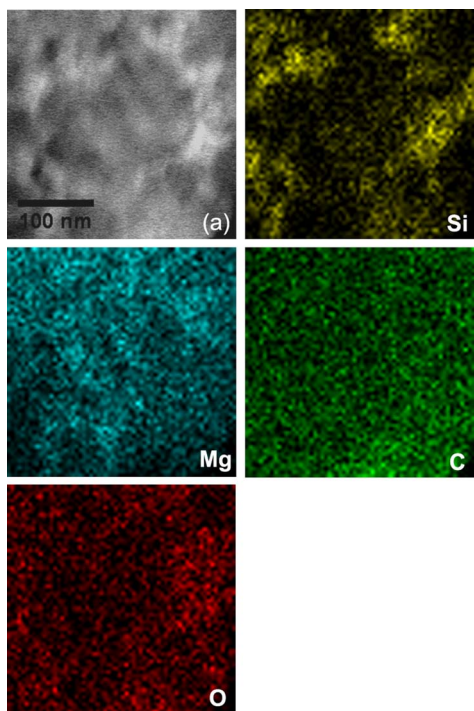


FIG. 7. (Color online) EDS elemental map of the 600 °C-10% SiC sample. (a) A Z-contrast image with a MgB₂ domain at the center and Si, Mg, C, and O maps of the same region.

again clear that the MgB₂ grain is practically surrounded by intragranular phases that are Si and O rich. O-rich regions have also been identified in pure MgB₂ samples, although less and smaller than in SiC-doped samples.

The C signal inside the MgB₂ indicates carbon doping, and is much smaller than it would be in the compound MgB₂C₂. Unfortunately, there is some buildup of hydrocarbons on the sample surface in the STEM, which makes it difficult to quantify the C concentration from this data. Similarly, the O signal from inside the MgB₂ domain in Fig. 6 may indicate some incorporation of O into the MgB₂, as has been reported in other samples,¹⁸ but it may also be due to surface oxidation of the sample after thinning for TEM.

In a separate experiment, pure Si pieces were glued to these MgB₂ samples during thinning for TEM, so that the surface hydrocarbon contamination rate could be estimated from the Si side. We then assume that the surface contamination is uniform across the whole sample and correct for its effects on the MgB₂ side. Since the results show lower C EELS intensity from Si pieces than from the MgB₂ pieces, we conclude that there is C doping of the MgB₂ in Fig. 6. Based on the differences between C intensity from Si pieces and from MgB₂ pieces, we used standard EELS quantification methods¹⁹ to estimate the C concentration in the MgB₂ lattice. In the formula Mg(B_xC_{1-x})₂, $x=1.5\pm 3\%$ for the 600 °C-10% SiC sample and $x=2.1\pm 5\%$ for the 900 °C-10% SiC sample from EELS. The large standard deviations are due to inhomogeneities in doped samples and uncertainties in the contamination rate subtract, but the EELS quantification results are remarkably close to the C concentration derived from the change in lattice parameter

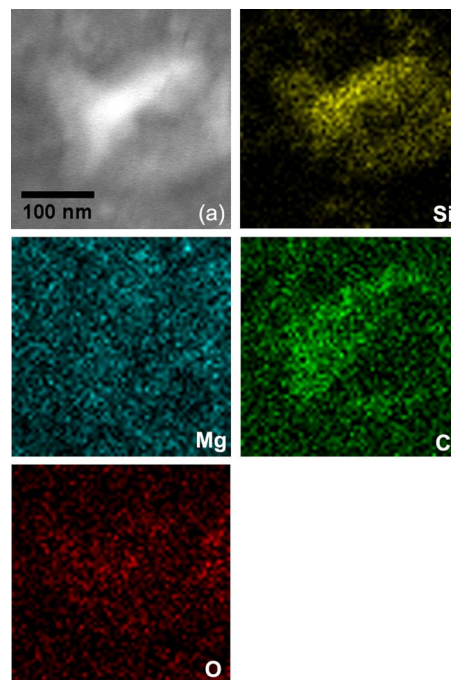


FIG. 8. (Color online) EDS elemental map of the 600 °C-10% SiC sample. (a) A Z-contrast image with a second phase domain at the center and Si, Mg, C, and O maps of the same region.

measured by XRD and calibrated against C-doped single crystal results,²⁰ which yields $x\sim 1.4\%$ and 2.2% for 600 °C and 900 °C-10% SiC samples, respectively.

The bright regions in the Z-contrast images in Figs. 5–7 are various second phases. Figure 6 shows that the surfaces of the MgB₂ domain are rich in C and O. Figure 7 shows that the surfaces are also rich in Si, which has been essentially excluded from the MgB₂. Although the O and especially the C EDS maps have detector-limited sensitivity, Fig. 7 shows the same trend of smaller C and O concentration inside the MgB₂ than outside seen in the EELS results of Fig. 6. Figure 8 shows a Z-contrast image of the 600 °C-10% SiC sample with one of the second-phase regions at the center and the corresponding EDS elemental maps. The bright domain is significantly Si rich and contains Mg, suggesting it might be Mg₂Si, but that is not consistent with the Z-contrast intensities of Table III, or with the enhanced C and O concentrations from the EDS maps. We are left with the conclusion that they are SiO_xC_y second phases, possibly also containing Mg, which we cannot quantitatively identify. These elemental maps show that Si atoms are rejected from MgB₂ domains and form second phases with C and O at the nanometer scale. From a positive point of view these particles are 50 nm or less and not superconducting, making them candidates for strong vortex pinning sites. But Figs. 5–7 also show that they cluster at grain boundaries, where they are capable of significantly degrading the connectivity from one grain to another and contributing to the small values of connectivity seen in Table I.

The results from the 900 °C-10% SiC sample are broadly similar. Figure 9 shows a Z-contrast image taken from the 900 °C-10% SiC sample and EELS and EDS elemental concentration results. We identify the bright region

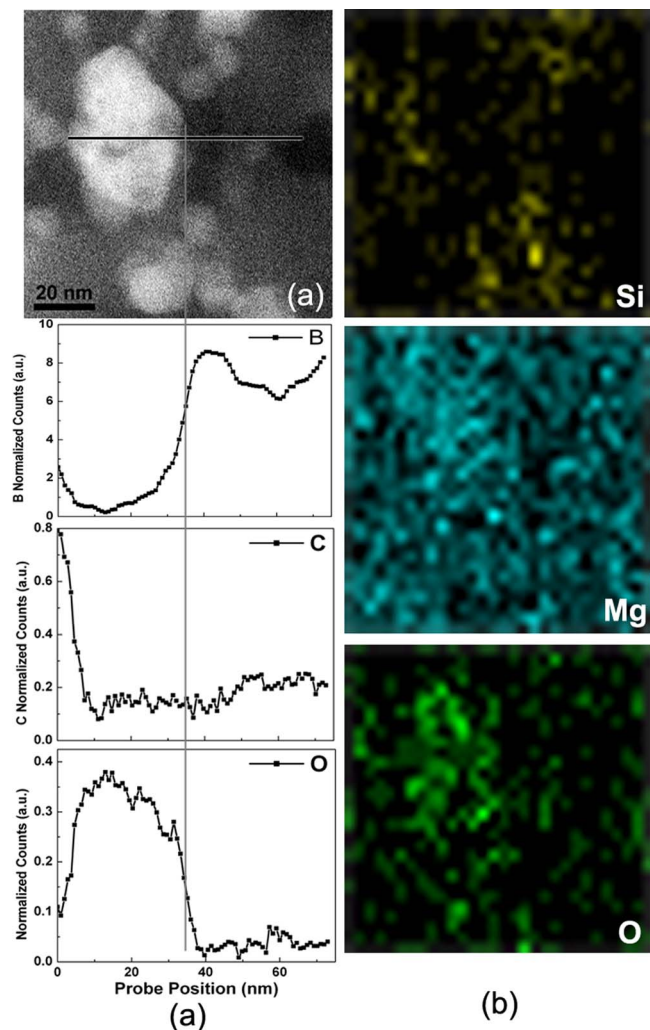


FIG. 9. (Color online) (a) Z-contrast image taken from 900 °C-10% SiC sample and the B, C, and O elemental distributions derived from an EELS line scan along the line in the image. EEL spectra were acquired every 1 nm. (b) Si, Mg, and O EDS elemental maps of the same region.

at the center of the image as an MgO particle, since it contains very little B or C and has a high concentration of O. EDS results confirm that there is very little Si but more Mg and O in this particle. In addition, the MgO particle in Fig. 9 shows less C than the neighboring MgB₂, confirming the conclusion drawn from C analysis of the Si/MgB₂ side-by-side sample that the C signal in Fig. 6 is due to C in the MgB₂ lattice, not just surface contamination.

Figure 10 shows two EEL spectra taken from the 900 °C-10% SiC sample, acquired at high enough dispersion for fine structure to be visible and with the low energy background before the Si *L*_{2,3} edge subtracted away. The core-level shifts and near-edge fine structure in these spectra are similar to published spectra²¹ of SiC or SiO_xC_y for the upper spectrum and SiO₂ for the lower spectrum. This shows that similar Si–O–C phases are present in both the 900 °C and 600 °C-10% SiC samples, and further that some of the Mg observed in Fig. 8 may not be in the bright second-phase particle, but instead above or below it in projection through the sample thickness.

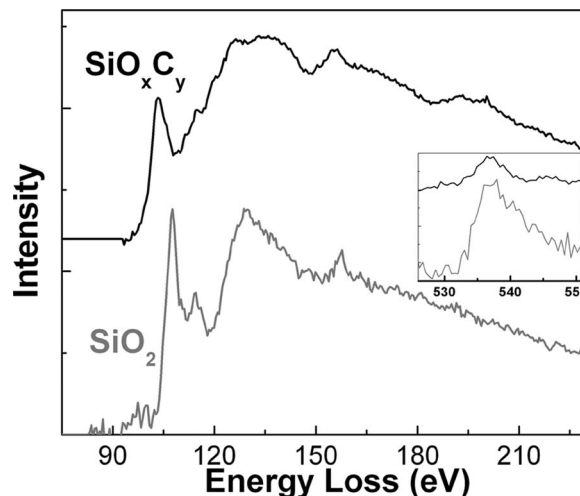


FIG. 10. Background-subtracted EEL spectra of the Si *L*_{2,3} edge of two different areas of the 900 °C-10% SiC sample. The upper spectrum shows fine structure and a core-level shift typical of SiO_xC_y, and the lower spectrum is typical of SiO₂. The inset shows the O *K* edge from the same two regions.

IV. DISCUSSION

A. Second phases

The second phases we have identified in the four samples are summarized in Table IV. Only MgO was found in the pure samples and even then only in very small quantities, leading us to conclude that synthesizing bulk MgB₂ from MgH₂ powder is promising as a way to reduce MgO contamination. As noted recently by Jiang *et al.*,¹⁴ O introduced as an unintended tramp with B can form extensive MgO nodules at grain boundaries that act as current blockers. However, the SiC nanoparticles in these samples apparently introduced significant additional oxygen, presumably as a surface adsorbed contaminant, which was not removed by the *in situ* reaction with MgH₂. This O then formed MgO, reaction products with Si, or other phases. Both 10% SiC-doped samples show stronger MgO diffraction and more O-rich regions in EDS and EELS than do the pure samples. Similar to the need to reduce the O contamination of B powder, it appears that prereducing the SiC powders would be beneficial to producing purer reactions and enhanced connectivity.

Besides MgO, we found various Si–O–C phases in the doped samples. In the 600 °C-10% SiC sample, Si is always found with both C and O, while in the 900 °C-10% SiC sample SiO₂ is identified explicitly by its EELS fine structure. This suggests more oxidation of Si at higher temperature. In both doped samples, Si–O–C phases are generally <50 nm in size and are dispersed between the MgB₂ grains,

TABLE IV. Second phases identified in MgB₂ tapes.

Samples	Identified phases	Possible phases
600 °C-pure	MgO (from EELS and EDS)	
600 °C-10% SiC	MgO, SiO _x C _y , Mg ₂ Si	SiC, MgB ₂ C ₂
900 °C-pure	MgO (from SAD and EDS)	
900 °C-10% SiC	MgO, SiO ₂ , SiO _x C _y	Mg ₂ Si, SiC, MgB ₂ C ₂

where they can be at least partially responsible for the anomalously large normal state resistivities seen in Table I. Large Mg_2Si grains, as shown in Fig. 4(b) in the 600 °C-10%SiC sample, were not found in the 900 °C-10%SiC sample, but their presence cannot be excluded due to the limited area it was possible to examine in TEM. We did not observe any large amorphous B pockets as reported by Hata *et al.*¹¹ in any of our samples.

The fact that we observe some C inside the MgB_2 but a higher concentration in the intergranular second phases suggests that the C has reached equilibrium in the MgB_2 and second phases at each reaction temperature; if so, our measured values of $x=0.015$ and 0.021 should represent the solid solubility of C in MgB_2+SiC system at 600 and 900 °C. Both EELS quantification and XRD analysis based on the change in lattice parameter²⁰ agree on these values. It is curious, however, that this is a significantly lower C concentration than the optimum of $0.04\text{--}0.05$ found in the higher temperature reaction studies using single crystals,⁴ CVD filaments,² and ball-milled C and MgB_2 .¹ In those cases there is good agreement both on the optimum value of x and that the optimum H_{c2} of bulk samples is ~ 35 T, rather than the ~ 42 T value found here for $x\sim 0.015$. We conclude that there are additional scattering centers present in these films, perhaps the defects seen within some grains (Fig. 3) and the many small grains and second phase particles with size 10–20 nm, much smaller than the clean mean free path of pure MgB_2 .

The small fraction of the cross sectional area available to carry current reported in Table I may be explained by the nonsuperconducting and generally insulating second phases present in all the samples and by the samples' high porosity. Porosity in these samples has been attributed to volume contraction during decomposition of MgH_2 , the escape of decomposed H_2 , and the volume contraction on reacting Mg and B.¹² There are more types of second phases and also more oxidation in the doped samples, which is consistent with their decreased connectivity. Figures 5–9 provide many examples of nonsuperconducting phases clustering at the grain boundary, where they must seriously degrade the connectivity. The increase of connectivity with increasing reaction temperature is less well explained. However, the average grain size at 900 °C is almost twice that at 600 °C, meaning that if the impurity phases occur at the same volume fraction, they should be less blocking due to smaller grain boundary area at higher temperature. Although most second phases are generally <50 nm in size and should therefore provide effective pinning force and enhance J_c , these samples show a lower J_c than earlier SiC-doped MgB_2 .⁶ The presence of Si–O phases limiting connectivity may be one of the reasons for this low J_c . This would be consistent with earlier work showing that SiO_2 does not increase J_c in tapes synthesized from MgH_2+B .¹²

B. H_{c2} and J_c

Figure 2 shows that the doped samples have higher H_{c2} than the pure ones and it is natural to consider that this must be due in part to C doping into the MgB_2 lattice. However,

the 600 °C-10% SiC sample has $H_{c2}(0\text{ K})\sim 42$ T, which is considerably higher than C-doped MgB_2 bulk materials^{1,2} and even the 600 °C-pure sample has $H_{c2}(0\text{ K})> 30$ T, one of the highest H_{c2} values reported in pure MgB_2 bulk material.⁵ This indicates that the low temperature reacted pure tapes contain more electron-scattering defects than MgB_2 tapes fabricated by other methods, a conclusion which is consistent with the lowered T_c values shown in Fig. 1. This disorder must have a comparable effect on H_{c2} to C doping, since the 600 °C-10% SiC sample has a higher H_{c2} than the 900 °C-10% SiC sample even though it has a lower C content ($x\sim 0.015$ vs 0.021). Table I shows that adding 10% SiC to MgB_2 tapes can increase $H_{c2}(10\text{ K})$ by 6–9 T, while lowering reaction temperature from 900 to 600 °C also increases H_{c2} by 5–8 T for both doped and pure samples. In addition to the very small grain size which may lead to significant grain boundary scattering, another source of scattering responsible for the enhanced H_{c2} values may be the extended intragrain defects visible in the TEM images of Fig. 3. Point disorder such as Mg vacancies or H in the MgB_2 lattice is also likely, but cannot generally be characterized by TEM or STEM. Both point and extended defects can be annealed out at high temperature, which is again consistent with the observation that H_{c2} decreases with increasing reaction temperature. In this picture, the very high H_{c2} of the 600 °C-10% SiC sample is caused by C substitution and by intrinsic lattice defects in the MgB_2 . But the breadth of the transition is large, suggesting considerable point-to-point variation of the properties.

The higher J_c values at $H>6$ T in doped samples indicate at least some of the second phases introduced by SiC addition act as effective pinning centers at high fields. This is also confirmed by the pinning force plot for these samples.⁷ The higher J_c in the 600 °C-pure sample compared to the 900 °C-pure sample is consistent with the smaller grain size associated with low temperature reacting (Fig. 3), as grain boundaries have been shown to be important pinning centers in MgB_2 films.²² On the other hand, larger grain boundary area may also lead to more second phase segregations which block the current flow and lower the grain connectivity. The poor connectivity values in Table I suggest that the local, vortex-pinning J_c of our samples is up to an order of magnitude higher.

This work shows that the lower the reaction temperature, the higher H_{c2} . Earlier work has shown that MgB_2 reaction occurs around 600 °C with the presence of SiC addition, which suggests that 600 °C is optimal heating temperature for the current $\text{MgH}_2+\text{B}+\text{SiC}$ system. This conclusion differs from that proposed of Sumption *et al.*, who used commercial Mg and B and found that 800 °C reactions were optimal for SiC-doped PIT MgB_2 wires.¹⁰ Such differences suggest that the fine nanostructural details presented here can vary considerably from one preparation method to another, and that they have multiple, complicated effects on scattering and connectivity which considerably complicate the optimization of MgB_2 for magnet applications.

V. CONCLUSIONS

MgB₂ tapes synthesized by powder-in-tube reaction at low temperature using MgH₂ as a Mg source and alloyed with SiC nanoparticles show exceptionally high $H_{c2}(0\text{ K}) > 40\text{ T}$. TEM analysis shows that synthesis with MgH₂ limits the formation of MgO in pure samples. Adding SiC inserts some C into the MgB₂ but also brings in O, which is presumably due to surface oxidization of the SiC nanoparticles. SiC also introduces Si-related second phases such as Mg₂Si and (Mg–)Si–O–C compounds. Various nonsuperconducting second phases enhance the high-field J_c by providing pinning, but also reduce the overall connectivity, which limits the measured J_c .

The grain size in all these samples is very small, providing strong grain boundary pinning and perhaps also the scattering that increases H_{c2} . The grain size nearly doubles between 600 and 900 °C reaction temperature. The higher reaction temperature also improves the connectivity. The very high H_{c2} of the 600 °C-10%SiC sample is caused by C doping, intrinsic lattice defects in the MgB₂, and the very fine grain structure. Due to the very complicated structure of these small-grain multiphase polycrystalline samples, it is difficult to identify the nature of the electron scattering defects and disorder, but our results suggest that removing surface O from the SiC nanoparticles would be beneficial to the superconducting properties.

ACKNOWLEDGMENTS

This work was supported by the US NSF FRG on MgB₂ (NSF Grant No. DMR-0514592). Three of the authors (A.M., H.K., and H.K.) were supported by the Ministry of Education, Culture, Sports, Science and Technology in Japan, and one of the authors (B.J.S.) was supported by the Fusion Energy Sciences Fellowship Program administered

by Oak Ridge Institute for Science and Education under contract between the U.S. DOE and the Oak Ridge Associated Universities.

- ¹B. J. Senkowicz, J. E. Giencke, S. Patnaik, C. B. Eom, E. E. Hellstrom, and D. C. Larbalestier, *Appl. Phys. Lett.* **86**, 202502 (2005).
- ²R. H. T. Wilke, S. L. Bud'ko, P. C. Canfield, D. K. Finnemore, R. J. Suplinskas, and S. T. Hannahs, *Phys. Rev. Lett.* **92**, 217003 (2004).
- ³A. Serquis, G. Serrano, S. M. Moreno, L. Civale, B. Maiorov, F. Balakirev, and M. Jaime, *Supercond. Sci. Technol.* **20**, L12 (2007).
- ⁴S. M. Kazakov *et al.*, *Phys. Rev. B* **71**, 024533 (2005).
- ⁵A. Gurevich *et al.*, *Supercond. Sci. Technol.* **17**, 278 (2004).
- ⁶S. X. Dou *et al.*, *Appl. Phys. Lett.* **81**, 3419 (2002).
- ⁷A. Matsumoto *et al.*, *Appl. Phys. Lett.* **89**, 132508 (2006).
- ⁸S. X. Dou, V. Braccini, S. Soltanian, R. Klie, Y. Zhu, S. Li, X. L. Wang, and D. C. Larbalestier, *J. Appl. Phys.* **96**, 7549 (2004).
- ⁹S. Li *et al.*, *Appl. Phys. Lett.* **83**, 314 (2003).
- ¹⁰M. D. Sumption, M. Bhatia, M. Rindfleisch, M. Tomsic, S. Soltanian, S. X. Dou, and E. W. Collings, *Appl. Phys. Lett.* **86**, 092507 (2005).
- ¹¹S. Hata, T. Yoshidome, H. Sosiati, Y. Tomokiyo, N. Kuwano, A. Matsumoto, H. Kitaguchi, and H. Kumakura, *Supercond. Sci. Technol.* **19**, 161 (2006).
- ¹²A. Matsumoto, H. Kumakura, H. Kitaguchi, and H. Hatakeyama, *Supercond. Sci. Technol.* **16**, 926 (2003).
- ¹³P. C. Canfield, S. L. Bud'ko, and D. K. Finnemore, *Physica C* **385**, 1 (2003).
- ¹⁴J. Jiang, B. J. Senkowicz, D. C. Larbalestier, and E. E. Hellstrom, *Supercond. Sci. Technol.* **19**, L33 (2006).
- ¹⁵J. M. Rowell, *Supercond. Sci. Technol.* **16**, R17 (2003).
- ¹⁶P. M. Voyles, J. L. Grazul, and D. A. Muller, *Ultramicroscopy* **96**, 251 (2003).
- ¹⁷S. Hillyard and J. Silcox, *Ultramicroscopy* **52**, 325 (1993).
- ¹⁸R. F. Klie, J. C. Idrobo, N. D. Browning, A. Serquis, Y. T. Zhu, X. Z. Liao, and F. M. Mueller, *Appl. Phys. Lett.* **80**, 3970 (2002).
- ¹⁹R. F. Egerton, *Electron Energy-Loss Spectroscopy in the Electron Microscope* (Plenum, New York, 1986).
- ²⁰S. Lee, T. Masui, A. Yamamoto, H. Uchiyama, and S. Tajima, *Physica C* **412–414**, 31 (2004).
- ²¹R. Schneider, J. Woltersdorf, and O. Lichtenberger, *J. Phys. D* **29**, 1709 (1996).
- ²²H. Kitaguchi, A. Matsumoto, H. Kumakura, T. Doi, H. Yamamoto, K. Saitoh, H. Sosiati, and S. Hata, *Appl. Phys. Lett.* **85**, 2842 (2004).